
Three-Dimensional Hydrodynamic Simulations of OMEGA Implosions

Introduction

Direct-drive inertial confinement fusion (ICF) experiments conducted at the 30-kJ Omega Laser Facility¹ are used to demonstrate the hydrodynamic equivalence of scaled-down cryogenic target implosions to ignition designs at MJ energies² such as those available at the National Ignition Facility.³ OMEGA implosion experiments demonstrate good agreement between the measured and simulated efficiency of conversion of the laser energy into the kinetic energy of the imploding shell (~4%). The fuel-compression stage of cryogenic implosions significantly underperforms, however, typically showing that the implosion's hot-spot pressure and deuterium–tritium (D–T) fusion neutron yield do not exceed ~60% of the values predicted in simulations using the one-dimensional (1-D) radiation–hydrodynamics code *LILAC*.⁴ This and other experimental evidence, including asymmetries of x-ray images of implosion shells and hot spots, nonspherical distribution of stagnated fuel shell ρR , and ~100-km/s directional motions of hot-spot plasma, both inferred from neutron measurements, suggest that short- and long-scale nonuniformities in implosion shells can cause the observed performance degradation.⁵

Short-scale nonuniformities (corresponding to Legendre modes $\ell \geq 30$) can be seeded by laser imprint⁶ and small target-surface and structural defects.⁷ The effects of Rayleigh–Taylor (RT) growth of these nonuniformities likely dominate over other effects of performance degradation in low-adiabat ($\alpha \lesssim 3$) and high in-flight aspect ratio (IFAR ≥ 25) implosions. Here, the adiabat α is defined in 1-D simulations as the ratio of the pressure in the imploding DT fuel shell to the corresponding Fermi-degenerated pressure and the IFAR is defined as the ratio of the shell's radius to its thickness (at a density level of 1 g/cm^3) at the moment when the ablation radius equals $2/3$ of the initial radius of the inner shell.⁸ The short-scale RT-growth effects can be mitigated using mid- to high-adiabat ($\alpha \geq 4$) and/or low-IFAR (≤ 20) implosions.⁸

Large-scale nonuniformities (with modes $\ell \lesssim 10$) can develop because of laser illumination and structural asym-

metries of implosion targets. The asymmetry of illumination is caused by the OMEGA laser's 60-beam-port configuration in addition to target offset (~10 to 20 μm) and inaccuracy of pointing, power balance, and timing of the beams (with typical $\sigma_{\text{rms}} < 10 \mu\text{m}$, 10%, and 5 ps, respectively). The structural asymmetries include mounting stalks,⁹ variations of thickness and shape of plastic (CH or CD) ablator shells in warm and cryogenic targets (with $\sigma_{\text{rms}} < 1 \mu\text{m}$), and variations in thickness of the DT ice layer in cryogenic targets (with $\sigma_{\text{rms}} \sim 1 \mu\text{m}$). Large-scale modes are amplified by the secular and Bell–Plesset¹⁰ growths and by the RT growth during the deceleration and stagnation stages. Variations of α and IFAR have little effect on the growth of these modes.

Investigation of the effects of large-scale asymmetries and the development of strategies to mitigate them are important steps toward improving the performance of OMEGA implosions. To understand these effects, experimental observations of implosion asymmetries are simulated in detail employing the three-dimensional (3-D) radiation–hydrodynamics code *ASTER*.¹¹ Results of 3-D simulations are post-processed to be directly compared with observables, which include x-ray images and deuterium–deuterium (DD) and/or DT fusion neutron spectra, among others.

This article describes recent progress in 3-D *ASTER* simulations of room-temperature and cryogenic OMEGA implosions focusing on large-scale ($\ell \lesssim 10$) target asymmetries as sources of the degradation in implosion performance. Simulations show that mode 1 is typically the most-destructive one in the case of both room-temperature and cryogenic implosions. The presence of this mode results in relatively large residual kinetic energy of implosion shells at maximum compression in comparison with that resulting from other modes (≥ 2) of similar amplitude. This large residual kinetic energy causes undercompression of the hot spot and a reduction of neutron yields down to values found in experiments. Mode 1 can be observed as an offset of the core emission in x-ray images with respect to the initial target center and as a directional variation of neutron spectra.

All above-mentioned sources of long-scale nonuniformities (except for that caused by the OMEGA discrete-beam illumination,¹¹ which introduces a dominant mode $\ell = 10$) can contribute to mode-1 perturbations. Mount stalks and target off-sets apparently result in such perturbations. Beam mistiming, mispointing, and imbalance, as well as initial target structural asymmetry, can be considered as quasi-random sources and result in perturbations having broad spectra, which peak at the lowest modes from 1 to ~ 3 and gradually decline toward higher modes. Recent 3-D simulations suggest that the latter sources can be important contributors to mode-1 asymmetries.

The goal of this work is to estimate the relative importance of different sources of large-scale nonuniformities in developing asymmetries in OMEGA implosions. This will help to specify improvements in both the OMEGA laser and target fabrication that can lead to improved implosion performance and a better understanding of the physics and robustness of the laser direct-drive approach. Understanding the sources of nonuniformities requires 3-D simulations assuming laser illumination and initial target structural asymmetries that are suggested by direct and indirect measurements and pre-shot target characterization. Results of these simulations are compared with asymmetries of implosion shells measured at different evolution stages, ranging from the beginning of shell acceleration until bang time.

The following sections (1) briefly describe the code *ASTER* and recent developments; (2) present results of 3-D *ASTER* simulations of room-temperature and cryogenic implosions and compare these results with experiments; and (3) present our discussion and conclusions.

The Numerical Method

Large-scale nonuniformities in OMEGA implosions were simulated using the 3-D radiation–hydrodynamics code *ASTER*. This code was tested against 1-D *LILAC* and two-dimensional (2-D) *DRACO*¹² results, showing good agreement with both results.¹¹

ASTER is an Eulerian code implemented on a spherical grid. Its hydrodynamic algorithm is based on the piecewise-parabolic Godunov method.¹³ This code uses a 3-D simplified laser-deposition model, which assumes inverse bremsstrahlung for light absorption and includes cross-beam energy transfer (CBET),¹⁴ and electron and ion Spitzer thermal transport¹⁵ without flux limitation. *ASTER* can use various on-the-fly and post-processing diagnostic routines that simulate, for example, neutron spectra and images, burn history, x-ray images, etc.

ASTER is characterized by low numerical noise that allows one to simulate nonuniform implosions without using any kind of diffusion or Fourier filtering to reduce the noise. Figure 149.1

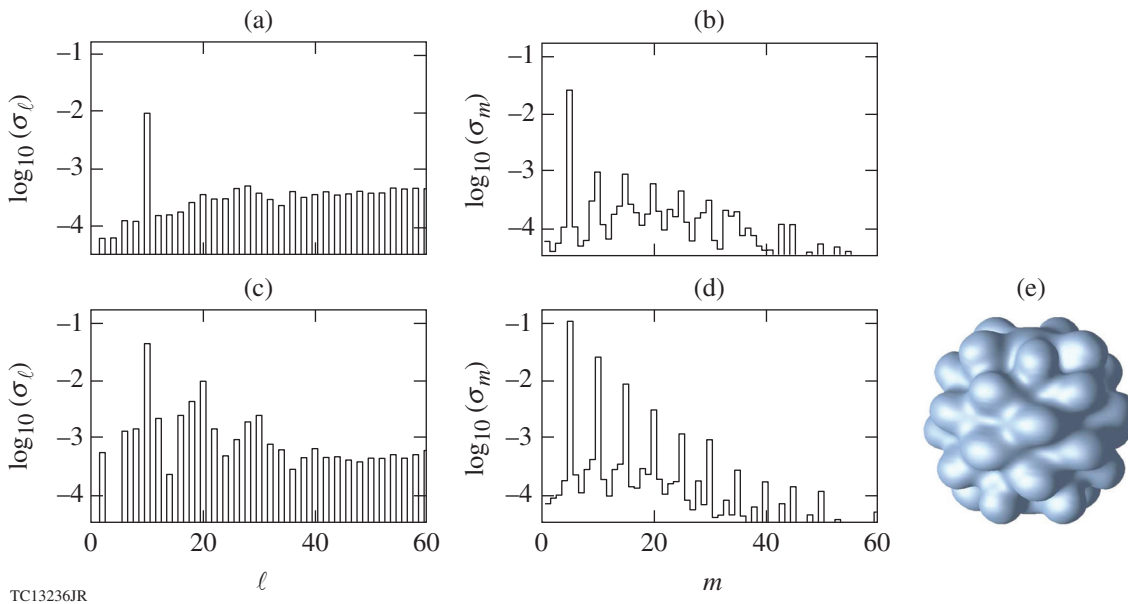


Figure 149.1

Three-dimensional *ASTER* test simulation assuming 1% perturbation of the mode $(\ell, m) = (10, 5)$ in laser deposition. [(a),(b)] The power spectra σ_ℓ and σ_m [see Eq. (1)] of the areal-density perturbation, respectively, at the end of the laser pulse, $t = 2.52$ ns; [(c),(d)] these spectra at $t = 2.805$ ns, which corresponds to $t_{\text{bang}} + 30$ ps. (e) An illustration of the shape of the hot spot at the latter time showing an isosurface of $T_i = 1$ keV.

shows example simulations of OMEGA cryogenic shot 77066 (see **Cryogenic Implosions**, p. 7) assuming a 1% perturbation of mode $(\ell, m) = (10, 5)$ in laser deposition. This simulation uses a numerical grid of 64×128 zones in the θ and ϕ dimensions, respectively. Figures 149.1(a)–149.1(c) show resulting normalized power spectra σ_ℓ and σ_m of the angular distribution of the areal density. These spectra are defined as follows:

$$\sigma_\ell = \sqrt{\sum_{m=-\ell}^{\ell} \sigma_{\ell, m}^2} \quad \text{and} \quad \sigma_m = \sqrt{\sum_{\ell=1}^{\ell_{\max}} \sigma_{\ell, m}^2}, \quad (1)$$

where $\sigma_{\ell, m}^2 = (C_{\ell, m}/C_{00})^2$ and $C_{\ell, m}$ are the expansion coefficients on the real (tesseral) spherical harmonics. Figures 149.1(a) and 149.1(b) show these spectra at the end of the laser pulse, $t = 2.52$ ns, when the shell’s implosion velocity approaches its maximum. One can see in these figures that the fundamental modes $\ell = 10$ and $m = 5$ dominate by more than an order of magnitude over the level of background noise introduced by numerical effects. At this time, the fundamental mode experiences mainly secular growth and is insignificantly affected by RT growth because of its relatively large wavelength. Figures 149.1(c) and 149.1(d) show the same spectra at $t = 2.805$ ns, which is about 30 ps after bang time, or peak neutron rate. At this time the shell is at maximum compression and is just beginning to move outward. Here, the shell undergoes an efficient RT growth and the perturbations become nonlinear, so that harmonics with $\ell = 20, 30$, and 40 and $m = 10, 15, \dots$ are clearly visible and dominate over the background noise. These harmonics are still, however, below the amplitude of the fundamental mode $(\ell, m) = (10, 5)$. Figure 149.1(e) shows the 3-D structure of the hot spot at $t = 2.805$ ps, represented by a 1-keV ion temperature isosurface.

Recent developments of *ASTER* include the capability to simulate radiation transport using multigroup flux-limited diffusion.¹⁶ This development is important since it makes it possible to accurately simulate room-temperature plastic-shell implosions, in which radiative ablation of the inner edge of the dense shell at maximum compression is important. Radiation transport is implemented using the parallel geometric multigroup algorithm.¹⁷ The use of spherical grids with anisotropies near the poles and typically higher resolution in the radial direction (versus angular directions) requires modifications to the standard multigroup relaxation and coarsening procedures to retain optimal efficiency.¹⁸ To treat the polar anisotropies, the algorithm uses nonuniform coarsening strategies, in which the grid is coarsened only in regions and directions that have sufficient isotropic grid coverage. This is combined with line

relaxation (using the marching algorithm) in the radial direction. The algorithm is adapted for parallel calculations using a domain decomposition approach similar to that used in the hydrodynamic part of *ASTER*.¹¹ Intensive test simulations have been performed to check the accuracy of the radiation-transport routine in *ASTER*. Results of these simulations showed good agreement with corresponding results obtained using *LILAC* and *DRACO*.

Simulation Results

The goal of this study is to identify the effects of large-scale asymmetries in OMEGA implosions with the help of 3-D simulations including a variety of nonuniformities in laser illumination and target structure. The nonuniformities can be chosen only to investigate their effects based on measurements. In the latter case, simulation results are compared with experiments.

Laser-induced nonuniformities include those created by the OMEGA beam-port geometry, target offset, and beam power imbalance, mistiming, and mispointing. The initial target structure nonuniformities can be caused by a variation in the thickness and shape of plastic shells in room-temperature and cryogenic targets and DT-ice shells in cryogenic targets.

The effects of beam imbalance and mistiming in *ASTER* simulations are included by using the power history of individual laser beams measured on a particular shot. This history is measured before laser light enters the target chamber; therefore, it can be different from the actual on-target value, which is affected by beam-forming optics and protective blast windows. The effects of the latter two are included in simulations by applying time-independent “imbalance correction” factors, which increase or reduce the power of individual beams. These factors are inferred using cross-calibration analysis of time-integrated x-ray images of laser spots from all 60 beams illuminating 4-mm-diam gold sphere targets with a 1-ns square pulse.¹⁹ These targets are chosen to be larger than the nominal OMEGA targets (with radius $R_t = 430 \mu\text{m}$) to avoid the overlapping of laser spots (with radius $R_b \approx 430 \mu\text{m}$). The imbalance correction factors are typically determined with the accuracy corresponding to about 1% to 2% of the beam power.

Beam mispointing is inferred using the same x-ray data from 4-mm-diam gold targets as in the case of the imbalance measurements.¹⁹ The mispointing data are determined with the accuracy of $\sim 5 \mu\text{m}$ and assumed to be fixed in time. These data are provided as horizontal (δx) and vertical (δy) displacements of laser spots with respect to their nominal positions on the target surface. *ASTER* models beam mispointing by

displacing the deposition regions for each beam by the angles of $\delta\theta = \delta y/R_{\text{dep}}$ and $\delta\phi = \delta x/R_{\text{dep}}$ in the spherical coordinates, where R_{dep} is the radius of the deposition region.

Target offset, or displacement of target center with respect to the laser pointing center, is measured using x-ray imaging²⁰ with an accuracy of about ± 3 to $5 \mu\text{m}$. Offsets are typically small for warm implosions ($< 5 \mu\text{m}$) and can be significant for cryogenic implosions (~ 10 to $20 \mu\text{m}$). *ASTER* models target offsets by displacing the deposition region of each beam by angles $\delta\theta$ and $\delta\phi$, which are calculated depending on the offset and its directionality and the radius R_{dep} .

Cryogenic and room-temperature targets are routinely used in OMEGA experiments to study implosion physics. While implosions of these targets share many common physical effects, there are important differences in experimental setups, initial target uniformity, and details of implosion physics that require separate considerations. First we will describe the *ASTER* simulations of room-temperature implosions. These simulations reproduce well the amplitude of observed asymmetries in implosion targets but not the directionality of these asymmetries. Next we will consider the results of cryogenic implosion simulations, which yield similar conclusions: there is good reproduction of the asymmetry amplitudes, but not directionality. The lack of agreement with the directionality can be explained by an inaccuracy of the assumed nonuniformities, which are measured within the time and space resolu-

tion of the diagnostics, while some of them are inferred from indirect measurements.

1. Room-Temperature Implosions

Room-temperature implosions have several advantages with respect to their cryogenic counterparts that make them a preferable choice for an initial study of large-scale asymmetries: (1) the relatively low fabrication and operation costs that result in an increased shot rate, (2) the ability to add high-Z dopants to the shell that is not fully ablated and confines fuel at stagnation, (3) smaller target offsets, and (4) relatively small initial target nonuniformities. The latter two allow one to concentrate on studying laser-induced asymmetries, whereas the ability to add dopants can help to quantify implosion core asymmetry using self-emission x-ray radiography.

Figure 149.2 shows two warm implosion designs that correspond to OMEGA shots (a) 79638 and (b) 79972. These designs have an IFAR ≈ 18 and 27 , respectively, and are relatively stable with respect to high-mode ($\ell \geq 30$) RT growth. Shot 79638 (a) uses a 10-atm D_2 -filled, $27\text{-}\mu\text{m}$ -thick plastic (CH) shell. Simulations of this shot are used to study implosion asymmetry during the laser drive and are compared with self-emission x-ray images (at $h\nu > 1 \text{ keV}$) of implosion shells.²¹ This x-ray emission comes mainly from a thin layer of plasma located immediately outside the ablation surface. Such images, therefore, can be used to measure the shape and outer radius of implosion shells.

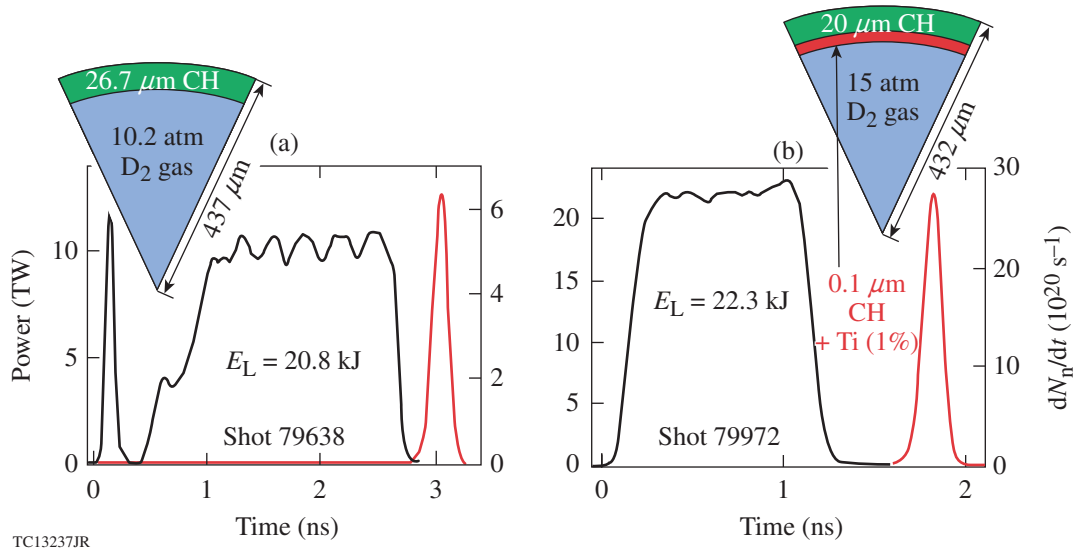


Figure 149.2

Schematic target structure, laser pulse (in black), and simulated neutron rate (in red, left axis) of two warm implosion designs corresponding to OMEGA shots (a) 79638 and (b) 79972.

The design in Fig. 149.2(b) (shot 79972) uses a 15-atm D₂-filled, 20- μm -thick plastic shell, which is doped by Ti (1% by atom) at the inner surface to a depth of $\sim 0.1 \mu\text{m}$. The purpose of this dopant is to characterize the shape and physical conditions at the fuel–ablator interface using Ti He β line emission (in the 5.45- to 5.65-keV x-ray band) at the time of hot-spot formation since this line emits at $T_e \gtrsim 1 \text{ keV}$ (Ref. 22).

Figures 149.3(a) and 149.3(b) compare experimental and simulated self-emission images, respectively, from shot 79638 at $t = 2.7 \text{ ns}$ (the TIM-5 viewing direction at $\theta = 100.8^\circ$ and $\phi = 270^\circ$ in the OMEGA coordinates). These images represent the shape of the ablation surface at the end of the acceleration phase. The simulations assume the known illumination nonuniformity seeds: OMEGA beam overlap and measured individual beam power histories (which introduce beam imbalance and mistiming) and mispointing (with $\sigma_{\text{rms}} \approx 16 \mu\text{m}$). The measured and simulated images were post-processed²³ to determine perturbations of the ablation surface. Figure 149.4 shows the evolution of the amplitude and phase of mode-2 perturbations in experiment and simulations. The measured mode-2 amplitude grows in time in good agreement with simulations [see Fig. 149.4(a)]. The mode-2 phases are almost independent in time in both experiment and simulations, but they are different by about 40° [see Fig. 149.4(b)]. The latter discrepancy in the phases suggests that the nonuniformity seeds assumed in simulations do not accurately represent the actual seeds.

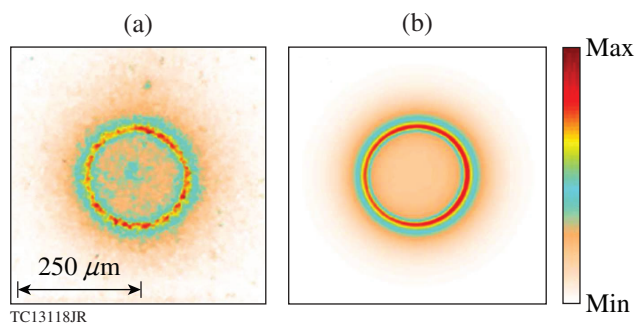


Figure 149.3
(a) Experimental and (b) simulated broadband x-ray ($h\nu > 1 \text{ keV}$), self-emission images of the implosion shell in shot 79638 at $t = 2.7 \text{ ns}$ (TIM-5 view).

Figures 149.5(a) and 149.5(b) compare experimental and simulated self-emission images of shot 79638 at $t = 2.9 \text{ ns}$ (in the same viewing direction as in Fig. 149.3). At this time, emissions from the ablation surface (outer ring) and from the core (center spot) are observed simultaneously. The offset of the core ($\sim 5 \mu\text{m}$), which is seen as a directional variation of the gap ΔR between the core edge and ablation surface edge in Fig. 149.5,

indicates significant mode-1 perturbations. The offset and its direction are in good agreement in both experimental and simulated images. Simulations show that this offset corresponds to mode-1 distortion of the implosion shell and fuel volume at bang time, as shown in Fig. 149.6. As a result, the simulated neutron yield 4.49×10^{10} is reduced to 43% of the yield of the corresponding uniform (1-D) implosion. This yield is a factor of 3 larger, however, than the measured yield $(1.79 \pm 0.09) \times 10^{10}$. Several factors explain the better-simulated performance: (1) an underestimation of the assumed nonuniformity seeds,

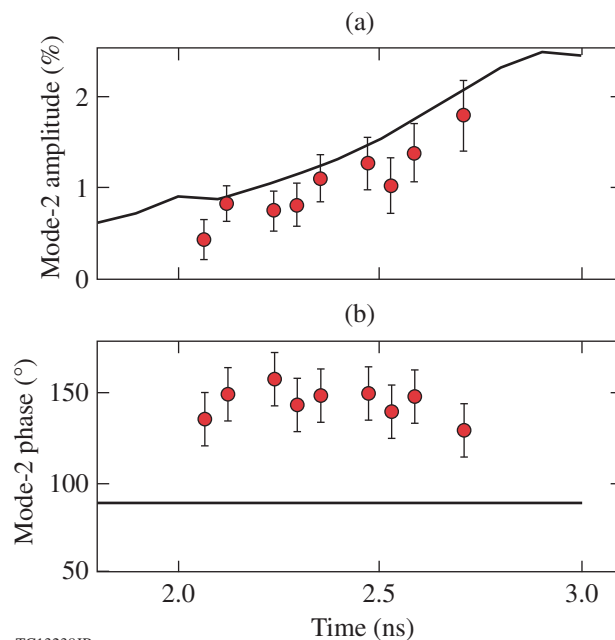


Figure 149.4
Evolution of (a) amplitude and (b) phase of mode-2 perturbations of the ablation surface in shot 79638 (TIM-5 view). Measurements are shown by red dots with error bars and simulations are shown by black lines.

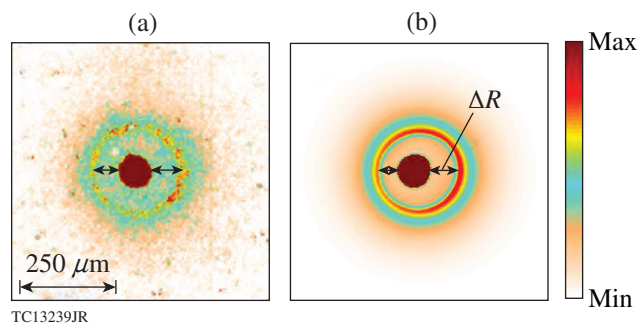


Figure 149.5
(a) Experimental and (b) simulated self-emission images of shot 79638 at $t = 2.9 \text{ ns}$. The offset of the emitting core (center spot) with respect to the image of the ablation surface (ring) represents the mode-1 perturbation.

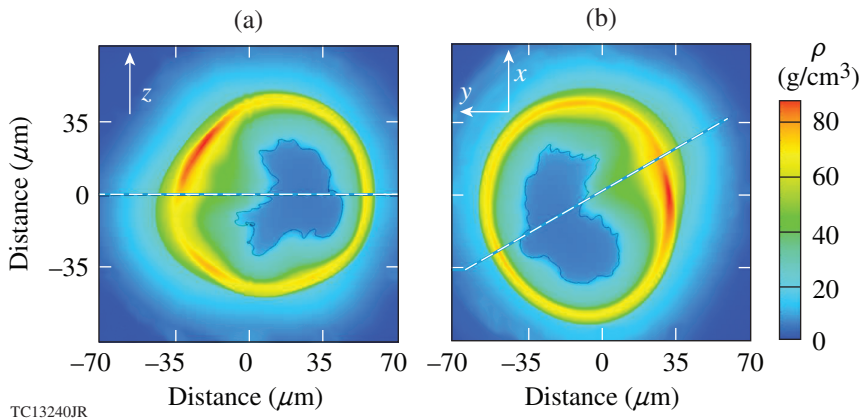


Figure 149.6
 (a) Meridional and (b) equatorial cross sections of the distribution of density from simulations of room-temperature shot 79638 at peak neutron production, $t = 3.02$ ns. The dashed line in (a) shows the equatorial plane and in (b) the location of the cross-section plane in (a). The solid line inside the dense shell shows the fuel–ablator (D–CH) interface.

(2) missing effects of small-scale mix that were not included in simulations; and/or (3) an inaccuracy in prescribing 1-D physics effects (laser absorption, CBET, heat transport, preheat, etc.).

Another example of significant mode-1 perturbation in OMEGA implosions is presented by shot 79972. Here, mode 1 was measured at a time near target stagnation. Figure 149.7 compares narrowband Ti He β emission images from this shot at two times, $t \approx t_{\text{bang}} - 100$ ps and $t \approx t_{\text{bang}}$. The emission limb, which corresponds to the location of the fuel–ablator (D–CH) interface, is consistently brighter on one side in both images, indicating the presence of dominant mode-1 asymmetry in the implosion core. The imager was located opposite the mounting stalk, so the limb asymmetry is unlikely to be caused by the stalk. There is a bright spot inside the limb, which is clearly observed in Fig. 149.7(a) at the earlier time and less clearly in Fig. 149.7(b) at the later time. This spot can be attributed to a jet that penetrates the hot spot and is introduced by the mounting assembly (stalk and glue spot).⁹

The observed mode-1 asymmetry in shot 79972 is likely caused by laser-illumination nonuniformities and can be quantified by comparing it with results of *ASTER* simulations. Figure 149.8 shows simulated distributions of the density and electron temperature in the equatorial cross section of shot 79972, assuming measured individual beam-power histories and pointing misalignment. The assumed perturbations result in mode-1 asymmetry of the dense CH-ablator shell and wide directional motion of the fuel material, which can be seen in Fig. 149.8 as distortion of the hot, low-density central volume occupied by this material. There is also a narrow, high-velocity jet moving in the same direction as the wide flow. This jet develops in the fuel material during successive bouncing of converging shocks produced by the shell during its deceleration. The yellow arrow in Fig. 149.8(a) indicates the directions

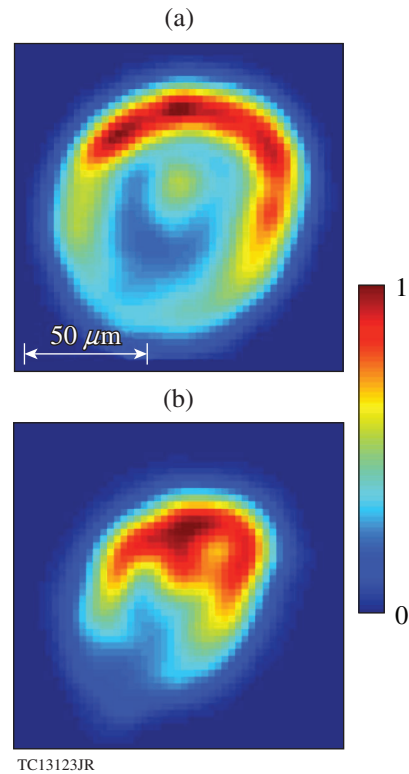


Figure 149.7
 Narrowband Ti He β (from 5.45 to 5.65 keV) images for shot 79972 at (a) $t \approx t_{\text{bang}} - 100$ ps and (b) $t \approx t_{\text{bang}}$. The view is opposite the position of the target-mounting stalk.

of the wide flow and jet and points to a dip in the ablator shell into which the jet “drills.”

The solid (color) line inside the dense shell in Fig. 149.8(a) shows the fuel–ablator interface, at which the Ti-doped material is concentrated [see Fig. 149.2(b)]. Simulated images of Ti He β line emission from this implosion are presented in Fig. 149.9.

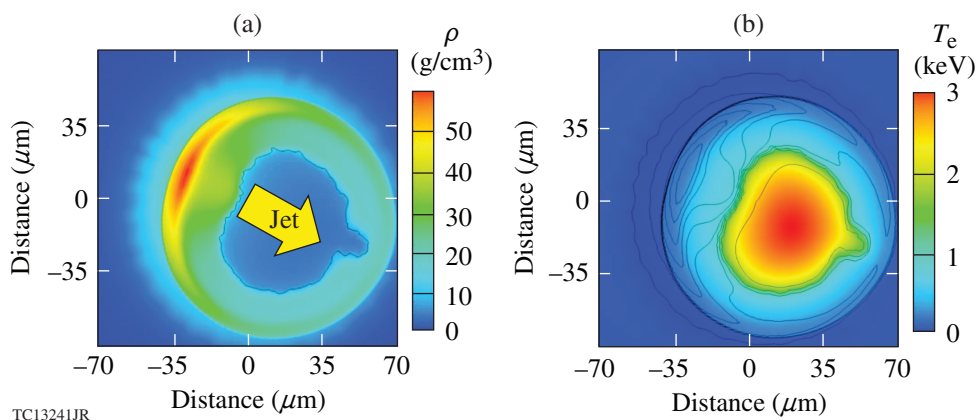


Figure 149.8

Equatorial cross sections of the distribution of (a) density and (b) electron temperature in simulations of shot 79972 at peak neutron production, $t = 1.785$ ns. The solid line in (a) shows the fuel-ablator interface where Ti-doped CH material is located. The arrow indicates the direction of a wide flow and jet, which develop in the hot-spot plasma because of the mode-1 perturbation. The solid lines in (b) show linearly spaced contours of the electron number density.

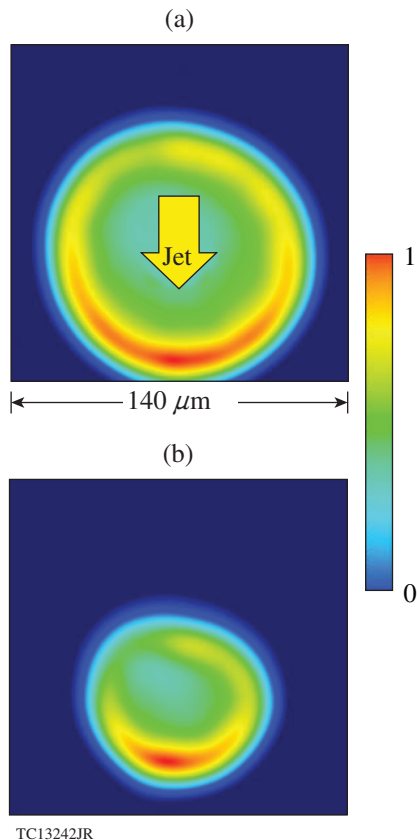


Figure 149.9

Simulated Ti He β images for shot 79972 at (a) $t = t_{\text{bang}} - 80$ ps and (b) $t_{\text{bang}} = 1.785$ ns. The viewing direction is from the pole and (b) corresponds to the distributions of density and electron temperature shown in Fig. 149.8, but at a different azimuthal orientation. The arrow in (a) points in the same direction of the jet in Fig. 149.8(a).

These images are calculated for the polar view and correspond to $t = t_{\text{bang}} - 80$ ps and $t = t_{\text{bang}}$, where $t_{\text{bang}} = 1.785$ ns [Figs. 149.9(a) and 149.9(b), respectively], and were produced by applying the same spatial (≈ 10 - μm) and temporal (≈ 40 -ps) smearing as in the experiment. The arrow in Fig. 149.9(a) shows the direction of the wide flow in the hot spot and corresponds to the same direction as in Fig. 149.8(a).

Simulations indicate that the asymmetry of the limb emission observed in shot 79972 (Fig. 149.7) is related to the wide directional motion of the fuel material caused by the mode-1 asymmetry of the shell. The brighter side of the emission limb develops in the direction of this motion. A detailed analysis shows that this brightening is mainly attributed to a local increase of T_e in the corresponding part of the fuel-ablator interface, while the role of variation in n_e is less significant [see Fig. 149.8(b)].

By comparing Figs. 149.7 and 149.9, one finds that while experiment and simulations show good agreement with respect to the amplitude of limb brightening, they disagree in directionality of this brightening. This disagreement is similar to that found in the simulations of shot 79638 (see Fig. 149.4) and confirms the claim that illumination nonuniformity seeds assumed in simulations do not accurately represent the real on-target seeds.

2. Cryogenic Implosions

Figure 149.10 shows a target schematic, pulse shape, and neutron history (from 1-D simulations) for shot 77066—one of the best-performing cryogenic OMEGA implosions—in which

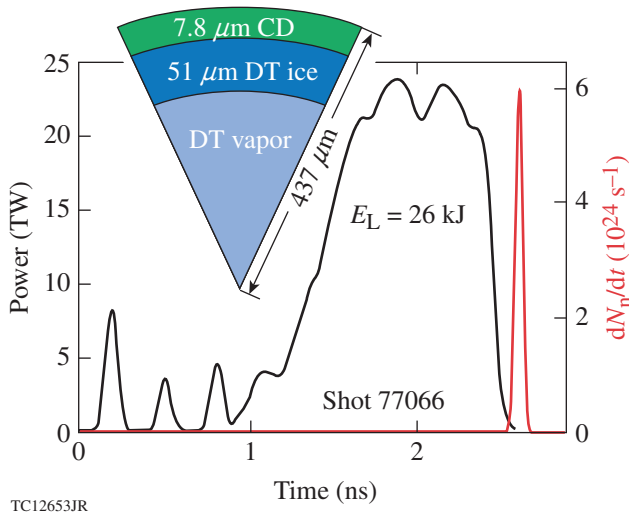


Figure 149.10
Schematic of the cryogenic capsule, laser pulse (black line), and simulated neutron rate (red line, right axis) for OMEGA shot 77066.

about 56 Gbar of hot-spot pressure was inferred.²⁴ This shot is characterized by an $\alpha \approx 3.2$ and IFAR ≈ 24 and should be relatively stable with respect to short-scale RT growth. The neutron yield, neutron-averaged (over DT neutrons) ion temperature $(T_i)_n$, and hot-spot pressure from uniform (1-D) *ASTER* simulations of this shot are 2.06×10^{14} , 3.39 keV, and 138 Gbar, respectively, and using *LILAC* they are 1.72×10^{14} , 3.67 keV, and 115 Gbar, respectively. *ASTER* simulations result in the absorption fraction of laser energy $f_{\text{abs}} = 0.54$ and bang time $t_{\text{bang}} = 2.66$ ns, while these results from *LILAC* are 0.60 and 2.68 ns, respectively. Table 149.I summarizes these results as well as the results of measurements. The discrepancies between the 1-D *ASTER* and *LILAC* results are relatively small and can be attributed to differences in the hydrodynamic methods used (Eulerian piecewise-parabolic method in *ASTER* and Lagrangian finite-difference scheme in *LILAC*) and the physical models (e.g., Spitzer versus nonlocal²⁵ heat transports, respectively).

Three-dimensional simulations of shot 77066 assume all sources of nonuniformities that can be currently quantified.

These include the power history of each individual beam, a target offset of $4 \mu\text{m}$ (in the direction of $\theta = 83^\circ$ and $\phi = 315^\circ$), and an ice-shell thickness variation with a mode-1 amplitude of $2 \mu\text{m}$ (oriented vertically, where the bottom is thinner), which were all measured in this shot. Simulations also assume beam-power imbalance correction factors and mispointing data (with $\sigma_{\text{rms}} = 8.5 \mu\text{m}$), which were measured in pointing shot 77059.

Figures 149.11(a) and 149.11(b) show, respectively, the equatorial and meridional (at $\phi = 83^\circ$) cross sections of the distribution of density at peak neutron production, $t = 3.572$ ns. Figure 149.12 shows a 3-D view of the hot spot at the same moment, where the hot-spot shape is represented by the isosurface $T_i = 900$ eV. The assumed sources of nonuniformities result in a distortion of the dense shell with the dominant mode 1. This mode can be clearly observed in Figs. 149.11(a) and 149.12 as an $\sim 10\text{-}\mu\text{m}$ shift of the dense shell and hot-spot centroids in the direction $\theta \approx 30^\circ$ and $\phi \approx 83^\circ$ with respect to the initial target center that was located at the origin. The shell is more dense on the side opposite the direction of the shift because of larger laser drive on that side resulting in higher convergence of the shell mass.

Simulations with the assumed asymmetries predict a yield of 8.07×10^{13} neutrons and $(T_i)_n = 3.03$ keV, therefore reducing the yield to 39% and $(T_i)_n$ to 89% of the corresponding values of uniform *ASTER* simulations. The measured neutron yield is $(3.9 \pm 0.2) \times 10^{13}$, which corresponds to 23% of the yield of *LILAC* simulations (see Table 149.I).

Neutron-averaged ion temperatures in OMEGA implosions are routinely inferred from DD and DT neutron spectra that include the thermal smearing and bulk motion effects in the hot spot.²⁶ In the case of cryogenic OMEGA implosions, DT neutron spectra are measured by detectors at three different directions: (1) $\theta = 84.98^\circ$ and $\phi = 311.76^\circ$, (2) $\theta = 87.86^\circ$ and $\phi = 161.24^\circ$, and (3) $\theta = 61.30^\circ$ and $\phi = 47.64^\circ$. These directions are indicated by the white dashed arrows in Fig. 149.11(a). The inferred ion temperatures in shot 77066 in these directions are

Table 149.I: Simulated and measured performance of OMEGA cryogenic shot 77066.

	Neutron yield	$(T_i)_n$ (keV)	P_{hs} (Gbar)	f_{abs} (%)	t_{bang} (ns)
<i>LILAC</i>	1.72×10^{14}	3.67	115	60	2.68
1-D <i>ASTER</i>	2.06×10^{14}	3.39	138	54	2.66
3-D <i>ASTER</i>	8.07×10^{13}	3.03	88	54	2.66
Experiment	$(3.9 \pm 0.2) \times 10^{13}$	N/A*	56 ± 7	58 ± 1	2.60 ± 0.05

* $(T_i)_n$ in the absence of bulk motion cannot be measured.

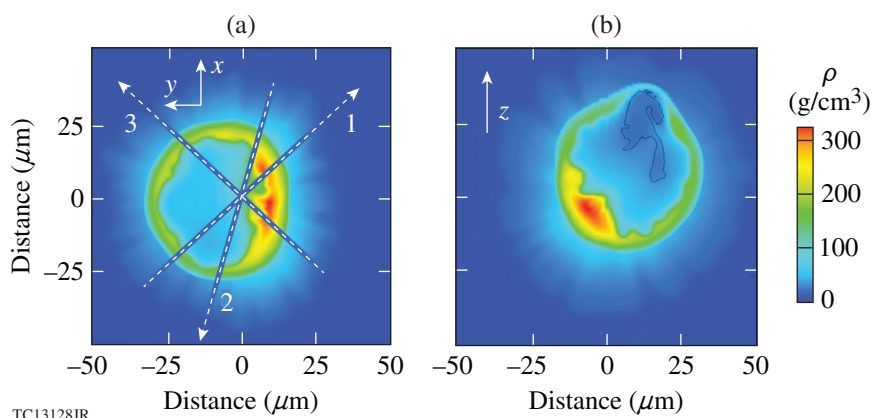


Figure 149.11
Distribution of density in simulations of shot 77066 in the (a) equatorial and (b) meridional (at $\phi = 83^\circ$) planes at peak neutron production, $t = 3.57$ ns. These simulations assume various nonuniformities in laser drive and initial target structure (see text). The white arrows show the coordinate axis indicating orientation of the images. The white dashed arrows show the three directions in which neutron data were collected.

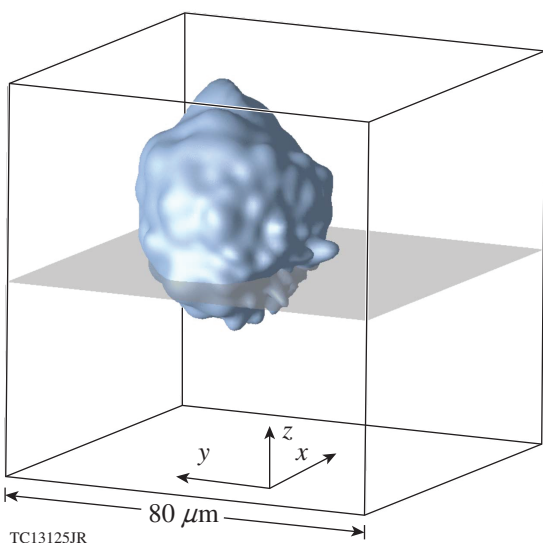


Figure 149.12
A 3-D view of the isosurface $T_i = 900$ eV, which represents the shape of the hot spot at peak neutron production in the same simulations as in Fig. 149.11. The cube with side sizes of $80 \mu\text{m}$ with the center at the origin and coordinate basis indicate spatial scale and orientation. The equatorial plane is shown in gray.

3.2 ± 0.2 , 3.8 ± 0.2 , and 3.6 ± 0.2 keV, respectively. Figure 149.13 shows simulated neutron spectra for the same directions, which are denoted by the numbers 1, 2, and 3, respectively. Gaussian fits to these spectra reveal ion temperatures of 3.9, 3.5, and 4.4 keV, respectively. These temperatures are substantially larger than simulated $(T_i)_n = 3.03$ keV, indicating significant bulk motion effects in the hot spot of this implosion. A comparison of these measured and simulated temperatures shows disagreements in their directional distributions. For example, the minimum and maximum temperatures are measured in directions 1 and 2 ($T_i = 3.2 \pm 0.2$ and 3.8 ± 0.2 keV, respectively), whereas simulations show those temperatures in directions 2 and 3 ($T_i = 3.5$ and 4.4 keV, respectively). On the other hand,

measurements and simulations show good agreement for the amplitude of directional variation of T_i ; the measured difference between the minimum and maximum temperatures is 0.6 keV, while the simulated difference is 0.9 keV. The latter agreement indicates that simulations correctly reproduce the actual magnitude of hot-spot asymmetry.

Shifts of the simulated neutron spectra in energy in Fig. 149.13 with respect to the unshifted energy of DT neutrons, $E_n = 14.1$ MeV, show a correlation with the direction of the hot-spot shift (see Fig. 149.11) caused by bulk motions. The spectra in red and green in Fig. 149.13 are shifted by $\Delta E \approx 40$ keV to smaller and larger energies, respectively. These spectral shifts are explained by negative and positive projection components

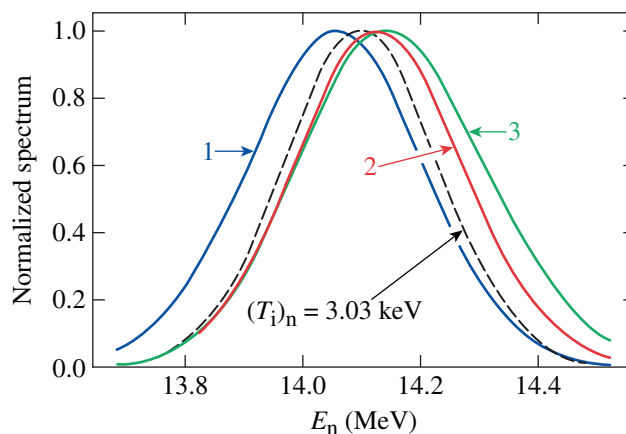


Figure 149.13
Simulated DT neutron spectra for shot 77066. The spectra in blue, red, and green (labeled 1, 2, and 3, respectively) were calculated for the three directions of OMEGA neutron diagnostics approximately indicated in Fig. 149.11(a) by the white dashed arrows (correspondingly labeled 1, 2, and 3). The hot-spot temperatures inferred from these spectra are 3.9, 3.5, and 4.4 keV, respectively. The black dashed line shows, for comparison, the Gaussian spectrum corresponding to $(T_i)_n = 3.03$ keV.

of the hot-spot motion (in the direction $\theta \approx 50^\circ$ and $\phi \approx 83^\circ$) in directions 1 and 3, respectively [see Fig. 149.11(a)]. Direction 2 is more perpendicular to the hot-spot motion and has a relatively small, positive projection component. This explains the relatively small shift of the spectrum shown in red in Fig. 149.13.

The spectral shifts in directions 1 and 3 correspond to the neutron-averaged hot-spot velocity components $\tilde{v}_f \sim \Delta E / \sqrt{2E_n m_n} \sim 70$ km/s. Correcting this estimate for an angle of $\sim 50^\circ$ between the hot-spot velocity and these directions [i.e., multiplying \tilde{v}_f by a factor of $\sim 1/\cos(50^\circ)$], one obtains an estimate of neutron-averaged velocity of the hot spot, $v_f \sim 110$ km/s. Simulations have found that the local flow velocity in the hot spot can substantially vary, taking the maximum value of about a factor of 5 larger than v_f in the hottest, low-density part of the hot spot. This part produces relatively fewer neutrons, however, and, therefore, insignificantly contributes to v_f . The shown example demonstrates the importance of spectral-shift measurements to understanding conditions in hot spots.

Discussion and Conclusions

Three-dimensional hydrodynamic simulations using the code *ASTER* were conducted to investigate sources of large-scale asymmetries in room-temperature and cryogenic OMEGA implosions. Simulations of room-temperature implosions were focused on studying the effects of laser-induced nonuniformities caused by OMEGA beam overlap, target offset, and beam imbalance, mispointing, and mistiming. It was shown that simulations assuming measured sources of these nonuniformities reproduce the amplitude of modes 1 and 2 observed in experiments at an earlier implosion evolution (up to the end of the laser pulse). The development of modes 1 and 2 was studied using self-emission x-ray radiography in up to three viewing directions. The phases of mode 2, however, were not correctly predicted in simulations. The latter indicates that the measured nonuniformity sources assumed in simulations do not accurately represent the actual sources.

Significant mode-1 asymmetry was observed in room-temperature implosions near the bang time. These implosions used plastic-shell targets, in which the inner edge of the shell was doped with titanium to a depth of $\sim 0.1 \mu\text{m}$. These targets start producing Ti He β line emission from the fuel–ablator interface when the temperature there exceeds ~ 1 keV. This emission forms bright limbs on x-ray images. Measurements typically find mode-1 asymmetry of the limb brightening, and this asymmetry is well reproduced in simulations assuming measured sources of illumination nonuniformity. The limb asymmetry is attributed to distortions of the dense shell and

hot spot with dominant mode 1, which is induced by laser illumination nonuniformities. Simulations suggest that the brighter limb side is developed in the direction of the hot-spot motion caused by these distortions; however, simulations do not reproduce the measured directionality of the limb brightening. This, again, indicates that the nonuniformity sources assumed in simulations do not accurately represent the actual sources.

To study the effects of large-scale asymmetry on performance degradation of cryogenic implosions, 3-D simulations of cryogenic shot 77066 were performed assuming the best currently known sources of the asymmetry. These sources were quantified and include the above-mentioned laser-illumination nonuniformities and nonuniformities caused by the target offset and variation in ice-shell thickness ($\approx 4 \mu\text{m}$ and $\pm 2 \mu\text{m}$ for mode 1, respectively). Simulations showed the development of dominant mode-1 asymmetry in the implosion shell at the time of maximum compression. This results in bulk motions in the hot spot with the neutron average velocity ~ 100 km/s in the direction that coincides with the direction of the mode-1 shell asymmetry. These motions result in a directional variation of the hot-spot temperature that is inferred from DT neutron spectra. The experimental and simulated temperatures show good agreement for the amplitude of this variation, but not for directionality of the maximum and minimum temperature measurements. The large-scale asymmetries result in a reduction of the simulated neutron yield to 39% of that of 1-D *ASTER* simulations, whereas the experimental yield shows 23% of the yield of *LILAC* simulations—a factor-of-about-2 overperformance in the simulation yields. This disagreement of the hot-spot temperature asymmetry in experiment and simulations suggests that it can be caused by an inaccuracy of the nonuniformity sources assumed in simulations.

Three-dimensional *ASTER* simulations of room-temperature and cryogenic OMEGA implosions show that large-scale asymmetries of the magnitudes observed in experiments can explain the measured performance degradation in mid- and high-adiabat implosions. Achieving better agreements between experiments and simulations will require a substantial improvement in the measurements of actual on-target nonuniformity sources that are assumed in simulations. In particular, current simulations assuming measured sources do not accurately reproduce directionality of low-mode perturbations (from modes 1 to 3), which limits the prediction capabilities of 3-D simulations.

A technique to correct the measured implosion shell asymmetry by modifying the power distribution of OMEGA

laser beams is under development. This technique uses a 3-D reconstruction of the shape of implosion shells with the help of self-emission x-ray radiography applied in several (three or more) viewing directions. Modifications of the beam-power distribution, which are based on *ASTER* predictions, will minimize the shell asymmetry and improve implosion performance.

The present study ignored the possibility that large-scale asymmetries in implosion shells can be affected by small-scale perturbations (with $\ell \gtrsim 50$) through mode coupling at the nonlinear stages of perturbation growth. The importance of this effect is unknown and will be studied in future works.

ACKNOWLEDGMENT

We thank D. Fyfe for suggestions that help to improve the radiation transport routine in *ASTER*. This material is based upon work supported by the Department of Energy National Nuclear Security Administration under Award Number DE-NA0001944, the University of Rochester, and the New York State Energy Research and Development Authority.

REFERENCES

1. T. R. Boehly, D. L. Brown, R. S. Craxton, R. L. Keck, J. P. Knauer, J. H. Kelly, T. J. Kessler, S. A. Kumpan, S. J. Loucks, S. A. Letzring, F. J. Marshall, R. L. McCrory, S. F. B. Morse, W. Seka, J. M. Soures, and C. P. Verdon, *Opt. Commun.* **133**, 495 (1997).
2. S. Atzeni and J. Meyer-ter-Vehn, *The Physics of Inertial Fusion: Beam Plasma Interaction, Hydrodynamics, Hot Dense Matter*, International Series of Monographs on Physics (Clarendon, Oxford, 2004).
3. E. I. Moses *et al.*, *Phys. Plasmas* **16**, 041006 (2009).
4. J. Delettrez, R. Epstein, M. C. Richardson, P. A. Jaanimagi, and B. L. Henke, *Phys. Rev. A* **36**, 3926 (1987).
5. V. N. Goncharov, S. P. Regan, E. M. Campbell, T. C. Sangster, P. B. Radha, J. F. Myatt, D. H. Froula, R. Betti, T. R. Boehly, J. A. Delettrez, D. H. Edgell, R. Epstein, C. J. Forrest, V. Yu. Glebov, D. R. Harding, S. X. Hu, I. V. Igumenshchev, F. J. Marshall, R. L. McCrory, D. T. Michel, W. Seka, A. Shvydky, C. Stoeckl, W. Theobald, and M. Gatu-Johnson, *Plasma Phys. Control. Fusion* **59**, 014008 (2017).
6. P. B. Radha, V. N. Goncharov, T. J. B. Collins, J. A. Delettrez, Y. Elbaz, V. Yu. Glebov, R. L. Keck, D. E. Keller, J. P. Knauer, J. A. Marozas, F. J. Marshall, P. W. McKenty, D. D. Meyerhofer, S. P. Regan, T. C. Sangster, D. Shvarts, S. Skupsky, Y. Srebro, R. P. J. Town, and C. Stoeckl, *Phys. Plasmas* **12**, 032702 (2005).
7. I. V. Igumenshchev, V. N. Goncharov, W. T. Shmayda, D. R. Harding, T. C. Sangster, and D. D. Meyerhofer, *Phys. Plasmas* **20**, 082703 (2013).
8. V. N. Goncharov, T. C. Sangster, R. Betti, T. R. Boehly, M. J. Bonino, T. J. B. Collins, R. S. Craxton, J. A. Delettrez, D. H. Edgell, R. Epstein, R. K. Follet, C. J. Forrest, D. H. Froula, V. Yu. Glebov, D. R. Harding, R. J. Henchen, S. X. Hu, I. V. Igumenshchev, R. Janezic, J. H. Kelly, T. J. Kessler, T. Z. Kosc, S. J. Loucks, J. A. Marozas, F. J. Marshall, A. V. Maximov, R. L. McCrory, P. W. McKenty, D. D. Meyerhofer, D. T. Michel, J. F. Myatt, R. Nora, P. B. Radha, S. P. Regan, W. Seka, W. T. Shmayda, R. W. Short, A. Shvydky, S. Skupsky, C. Stoeckl, B. Yaakobi, J. A. Frenje, M. Gatu-Johnson, R. D. Petrasso, and D. T. Casey, *Phys. Plasmas* **21**, 056315 (2014).
9. I. V. Igumenshchev, F. J. Marshall, J. A. Marozas, V. A. Smalyuk, R. Epstein, V. N. Goncharov, T. J. B. Collins, T. C. Sangster, and S. Skupsky, *Phys. Plasmas* **16**, 082701 (2009).
10. G. I. Bell, Los Alamos National Laboratory, Los Alamos, NM, Report LA-1321 (1951); M. S. Plesset, *J. Appl. Phys.* **25**, 96 (1954).
11. I. V. Igumenshchev, V. N. Goncharov, F. J. Marshall, J. P. Knauer, E. M. Campbell, C. J. Forrest, D. H. Froula, V. Yu. Glebov, R. L. McCrory, S. P. Regan, T. C. Sangster, S. Skupsky, and C. Stoeckl, *Phys. Plasmas* **23**, 052702 (2016).
12. P. B. Radha, T. J. B. Collins, J. A. Delettrez, Y. Elbaz, R. Epstein, V. Yu. Glebov, V. N. Goncharov, R. L. Keck, J. P. Knauer, J. A. Marozas, F. J. Marshall, R. L. McCrory, P. W. McKenty, D. D. Meyerhofer, S. P. Regan, T. C. Sangster, W. Seka, D. Shvarts, S. Skupsky, Y. Srebro, and C. Stoeckl, *Phys. Plasmas* **12**, 056307 (2005).
13. P. Colella and P. R. Woodward, *J. Comput. Phys.* **54**, 174 (1984).
14. I. V. Igumenshchev, D. H. Edgell, V. N. Goncharov, J. A. Delettrez, A. V. Maximov, J. F. Myatt, W. Seka, A. Shvydky, S. Skupsky, and C. Stoeckl, *Phys. Plasmas* **17**, 122708 (2010).
15. L. Spitzer, Jr. and R. Härm, *Phys. Rev.* **89**, 977 (1953).
16. D. Mihalas and B. Weibel-Mihalas, *Foundations of Radiation Hydrodynamics* (Oxford University Press, New York, 1984).
17. W. L. Briggs, V. E. Henson, and S. F. McCormick, *A Multigrid Tutorial*, 2nd ed. (Society for Industrial and Applied Mathematics, Philadelphia, 2000).
18. S. Buckeridge and R. Scheichl, *Numer. Linear Algebr* **17**, 325 (2010).
19. F. J. Marshall, J. A. Delettrez, R. Epstein, R. Forties, R. L. Keck, J. H. Kelly, P. W. McKenty, S. P. Regan, and L. J. Waxer, *Phys. Plasmas* **11**, 251 (2004); R. A. Forties and F. J. Marshall, *Rev. Sci. Instrum.* **76**, 073505 (2005).
20. W. Grimble, F. J. Marshall, and E. Lambrides, "Measurement of Cryogenic Implosion Core Offsets in OMEGA's Inertial Confinement Fusion Experiments," to be submitted to Review of Scientific Instruments.
21. D. T. Michel, C. Sorce, R. Epstein, N. Whiting, I. V. Igumenshchev, R. Jungquist, and D. H. Froula, *Rev. Sci. Instrum.* **83**, 10E530 (2012).
22. R. C. Shah, B. M. Haines, F. J. Wysocki, J. F. Benage, J. Fooks, V. Glebov, P. Hakel, M. Hoppe, I. V. Igumenshchev, G. Kagan, R. C. Mancini, F. J. Marshall, D. T. Michel, T. J. Murphy, M. E. Schoff, C. Stoeckl, and B. Yaakobi, "Systematic Fuel Cavity Asymmetries in Directly Driven ICF Implosions," to be published in Physical Review Letters.
23. D. T. Michel, A. K. Davis, W. Armstrong, R. Bahr, R. Epstein, V. N. Goncharov, M. Hohenberger, I. V. Igumenshchev, R. Jungquist, D. D. Meyerhofer, P. B. Radha, T. C. Sangster, C. Sorce, and D. H. Froula, *High Power Laser Science and Engineering* **3**, e19 (2015).

24. S. P. Regan, V. N. Goncharov, I. V. Igumenshchev, T. C. Sangster, R. Betti, A. Bose, T. R. Boehly, M. J. Bonino, E. M. Campbell, D. Cao, T. J. B. Collins, R. S. Craxton, A. K. Davis, J. A. Delettrez, D. H. Edgell, R. Epstein, C. J. Forrest, J. A. Frenje, D. H. Froula, M. Gatu Johnson, V. Yu. Glebov, D. R. Harding, M. Hohenberger, S. X. Hu, D. Jacobs-Perkins, R. T. Janezic, M. Karasik, R. L. Keck, J. H. Kelly, T. J. Kessler, J. P. Knauer, T. Z. Kosc, S. J. Loucks, J. A. Marozas, F. J. Marshall, R. L. McCrory, P. W. McKenty, D. D. Meyerhofer, D. T. Michel, J. F. Myatt, S. P. Obenshain, R. D. Petrasso, R. B. Radha, B. Rice, M. Rosenberg, A. J. Schmitt, M. J. Schmitt, W. Seka, W. T. Shmayda, M. J. Shoup III, A. Shvydky, S. Skupsky, S. Solodov, C. Stoeckl, W. Theobald, J. Ulreich, M. D. Wittman, K. M. Woo, B. Yaakobi, and J. D. Zuegel, *Phys. Rev. Lett.* **117**, 025001 (2016); **117**, 059903(E) (2016).
25. V. N. Goncharov, T. C. Sangster, P. B. Radha, R. Betti, T. R. Boehly, T. J. B. Collins, R. S. Craxton, J. A. Delettrez, R. Epstein, V. Yu. Glebov, S. X. Hu, I. V. Igumenshchev, J. P. Knauer, S. J. Loucks, J. A. Marozas, F. J. Marshall, R. L. McCrory, P. W. McKenty, D. D. Meyerhofer, S. P. Regan, W. Seka, S. Skupsky, V. A. Smalyuk, J. M. Soures, C. Stoeckl, D. Shvarts, J. A. Frenje, R. D. Petrasso, C. K. Li, F. Séguin, W. Manheimer, and D. G. Colombant, *Phys. Plasmas* **15**, 056310 (2008).
26. M. Gatu Johnson, J. A. Frenje, D. T. Casey, C. K. Li, F. H. Seguin, R. Petrasso, R. Ashabranner, R. M. Bionta, D. L. Bleuel, E. J. Bond, J. A. Caggiano, A. Carpenter, C. J. Cerjan, T. J. Clancy, T. Doeppner, M. J. Eckart, M. J. Edwards, S. Friedrich, S. H. Glenzer, S. W. Haan, E. P. Hartouni, R. Hatarik, S. P. Hatchett, O. S. Jones, G. Kyrala, S. Le Pape, R. A. Lerche, O. L. Landen, T. Ma, A. J. MacKinnon, M. A. McKernan, M. J. Moran, E. Moses, D. H. Munro, J. McNaney, H. S. Park, J. Ralph, B. Remington, J. R. Rygg, S. M. Sepke, V. Smalyuk, B. Spears, P. T. Springer, C. B. Yeamans, M. Farrell, D. Jasion, J. D. Kilkenny, A. Nikroo, R. Paguio, J. P. Knauer, V. Yu. Glebov, T. C. Sangster, R. Betti, C. Stoeckl, J. Magoon, M. J. Shoup III, G. P. Grim, J. Kline, G. L. Morgan, T. J. Murphy, R. J. Leeper, C. L. Ruiz, G. W. Cooper, and A. J. Nelson, *Rev. Sci. Instrum.* **83**, 10D308 (2012).